Published in final edited form as:
Magn Reson Med. 2014 May ; 71(5): 1798–1812. doi:10.1002/mrm.24850.

Variable Delay Multi-Pulse Train for Fast Chemical Exchange Saturation Transfer and Relayed-Nuclear Overhauser Enhancement MRI

Jiadi Xu[1,2,*], **Nirbhay N. Yadav**[1,2], **Amnon Bar-Shir**[1,3], **Craig K. Jones**[1,2], **Kannie W. Y. Chan**[1,2], **Jiangyang Zhang**[1,3], **P. Walczak**[1,3], **Michael T. McMahon**[1,2], and **Peter C. M. van Zijl**[1,2]

[1]Russell H. Morgan Department of Radiology and Radiological Science, Johns Hopkins University School of Medicine, Baltimore, Maryland, USA

[2]F.M. Kirby Research Center for Functional Brain Imaging, Kennedy Krieger Research Institute, Baltimore, Maryland, USA

[3]The Institute for Cell Engineering, Johns Hopkins University School of Medicine, Baltimore, Maryland, USA

Abstract

Purpose—Chemical exchange saturation transfer (CEST) imaging is a new MRI technology allowing the detection of low concentration endogenous cellular proteins and metabolites indirectly through their exchangeable protons. A new technique, variable delay multi-pulse CEST (VDMP-CEST), is proposed to eliminate the need for recording full Z-spectra and performing asymmetry analysis to obtain CEST contrast.

Methods—The VDMP-CEST scheme involves acquiring images with two (or more) delays between radiofrequency saturation pulses in pulsed CEST, producing a series of CEST images sensitive to the speed of saturation transfer. Subtracting two images or fitting a time series produces CEST and relayed-nuclear Overhauser enhancement CEST maps without effects of direct water saturation and, when using low radiofrequency power, minimal magnetization transfer contrast interference.

Results—When applied to several model systems (bovine serum albumin, crosslinked bovine serum albumin, L-glutamic acid) and in vivo on healthy rat brain, VDMP-CEST showed sensitivity to slow to intermediate range magnetization transfer processes (rate < 100–150 Hz), such as amide proton transfer and relayed nuclear Overhauser enhancement-CEST. Images for these contrasts could be acquired in short scan times by using a single radiofrequency frequency.

Conclusions—VDMP-CEST provides an approach to detect CEST effect by sensitizing saturation experiments to slower exchange processes without interference of direct water saturation and without need to acquire Z-spectra and perform asymmetry analysis.

[*]Correspondence to: Jiadi Xu, Ph.D., Department of Radiology, Johns Hopkins University School of Medicine, 217 Traylor Bldg, 720 Rutland Ave, Baltimore, MD 21205. XuJ@kennedykrieger.org.

Keywords

chemical exchange; CEST; magnetization transfer; MTC; contrast agent; exchange rate; pulsed CEST; rNOE-CEST; APT; VDMP-CEST; relayed NOE

Since Balaban and coworkers first proposed the term chemical exchange saturation transfer (CEST) in 2000 (1), CEST imaging has developed into a powerful technology with widespread interest in the MRI community (2–5). CEST imaging utilizes radiofrequency (RF) irradiation to selectively saturate solute protons. The saturation is transferred to water through rapid exchange of these protons, resulting in a reduction in water signal intensity (SI). If the exchange rate is sufficiently fast (residence time in millisecond range) and the irradiation period sufficiently long (seconds range), the low concentration saturated solute protons are mostly replaced by high concentration unsaturated water protons so that the saturation transfer process repeats many times during the course of the RF irradiation. Consequently, the selective irradiation of these solute protons can have a discernible effect on the water SI, which allows the indirect imaging of low-concentration solutes through water. Furthermore, the dependence of the CEST effect on the RF irradiation duration (t_{sat}) and strength (B_1) provides additional information on the kinetics of exchange, the concentration of the exchangeable protons, and the relaxation properties of water (6). This possibility to enhance sensitivity has led to a large variety of techniques developed for imaging low concentration diamagnetic compounds, such as glycosoaminoglycans (7), glucose/glycogen (8–10), glutamate (11), amino acids, peptides, and proteins (12–15), as well as paramagnetic lanthanide complexes (paraCEST) (16–19) and particles (20–23).

Among all the CEST techniques, the amide proton transfer (APT) approach, which targets the exchangeable amide protons in peptides and proteins, has become of particular interest because of several unique properties that make it favorable for in vivo application (12,24–27). These include (i) the high total concentration of amide protons of endogenous mobile proteins and peptides, corresponding to about 70 mM amide proton concentration found in the mammalian brain (12); (ii) sufficiently low interference from the water signal due to a relatively large chemical shift between amide and water protons (~3.6 ppm); (iii) the relatively slow exchange rate (~30 Hz) of these amide protons that allows the use of low power RF saturation pulses for their detection. To date, APT-weighted imaging has been successfully applied to detect tumors in the brain (24,28), prostate (29), and breast (30) in vivo in patients, and pH changes during ischemia in vivo in preclinical models (31–34).

In APT imaging, we are interested in the change in signal due to the chemical exchange of amide protons. However, similar to any saturation transfer based sequence, loss of signal can result from a number of competing mechanisms such as direct water saturation (DS), and conventional magnetization transfer contrast (MTC) from semi-solid macromolecules to water. CEST/APT experiments therefore generally require acquisition of a series of images as a function of irradiation frequency (Z-spectrum). This is followed by asymmetry analysis of the Z-spectrum with respect to the water proton frequency, in which the magnetization transfer ratio (MTR) obtained at the negative offset with respect to water is subtracted from the MTR at the corresponding positive offset. While the goal of this approach originally was

to remove the effects of DS and MTC, many investigators now realize that complete removal of MTC may not be possible in vivo, because MTC contrast is not completely symmetric about the water signal (35–38). In addition to MTC, it has been shown recently that contrast in Z-spectra also arises through transfer of saturation-induced nuclear Overhauser enhancements (NOEs) in mobile macromolecules between aliphatic/olefinic or aromatic protons, which can transfer to water either directly or relayed (2,7,39–41). Most of this signal is upfield from water (lower frequency), where the aliphatic and olefinic protons resonate. This NOE-CEST contrast is a two-stage process. First, nonexchangeable protons transfer their saturation-induced NOE via through-space dipolar coupling, and then the saturated magnetization is transferred to the water pool, most likely by chemical exchange as known from studies of the inverse exchange-relayed process in protein solution (42,43) and in vivo (26,44). Notice that, contrary to the semisolid MTC effect, direct dipolar exchange through space is unlikely to occur in small to intermediate size mobile proteins as that process is known to be much slower than chemical exchange (42,45). We therefore call this type of CEST contrast “relayed-NOE CEST” (rNOE-CEST) to distinguish it from direct exchange contrast. In addition to the rNOE effect, direct NOEs transferred through dipolar coupling between immobile water and aliphatic protons may become significant for larger molecules as suggested by a study on cartilage (7). The current technique focuses on the mobile proteins in vivo. Although, the direct NOE pathway cannot be excluded in mobile proteins, the rNOE pathway is dominant as suggested by studies using the water exchange filter (WEX) technique (25). The rNOE-CEST shares many properties with the APT contrast, but in principle has much stronger signal due to a greater number of aliphatic protons compared to amide protons. Therefore it has great potential for in vivo application.

The acquisition of detailed Z-spectra is time consuming. In addition, extra scans are often performed (e.g., water saturation shift referencing (46)) to allow for a voxel-based correction of the water proton frequency used as reference in the asymmetry analysis. The need to acquire Z-spectra and water saturation shift referencing-spectra poses a significant practical limitation for clinical translation of APT studies, because more signal averaging could take place (to enhance sensitivity) or the experiment time reduced if fewer frequencies were needed. Recently, faster methods have been suggested, including saturation with frequency alternating RF irradiation (SAFARI) (37), employing a frequency-alternating scheme requiring four acquisitions, and chemical exchange rotation transfer (CERT) (47), using two rotations, requiring only two acquisitions. Here, we propose a method for obtaining APT and rNOE-CEST contrast images called variable delay multi-pulse CEST (VDMP-CEST). This scheme is based on varying the delay (mixing time) between the RF pulses in a pulsed RF irradiation scheme (Fig. 1a). Only one irradiation frequency is used and only two images with different delay times need to be acquired, with the first image collected with delay equal to zero (reference image) and the second with a delay set to a value sufficient for weighting the images based on the appropriate magnetization transfer rate. The final VDMP-CEST image is then obtained by subtracting the long delay image from the reference image. When using sufficiently low B_1, effects from direct water saturation and very fast exchanging protons will be removed by the subtraction, while the effect of slower CEST processes such as APT and rNOE-CEST contrast are preserved with a magnitude much larger than conventional MTC. The reason for the latter is that a variable delay will

distinguish very short T_2 (MTC) and longer T_2 species (48) as well as faster and slower transfer processes in long-T_2 species. Here we first show how CEST and rNOE-CEST contrast changes as a function of mixing time in VDMP-CEST experiments for different exchangeable protons in several model compounds (glutamate (Glu), bovine serum albumin (BSA) and crosslinked BSA), followed by a demonstration in vivo in the rat brain.

Methods

Theory

In this section, we provide an overview of the possible magnetization transfer pathways for semi-solid protons and mobile peptide/protein protons and show how varying the pulse power and the inter-pulse delays can be used as a T_2 filter and exchange rate filter respectively. Finally, we discuss how using a proper combination of pulse power and inter-pulse delay can separate the APT and rNOE-CEST signals from other magnetization transfer pathways.

Magnetization Transfer Pathways in Tissue—The magnetization transfer process for water in tissue has contributions from many pools (Fig. 1b). One is the semi-solid macromolecular pool (microsecond T_2) giving rise to the conventional MTC effect (49), and another the mobile macromolecular pool of mainly proteins/peptides (millisecond range T_2), which, together with many metabolite pools, contributes to the endogenous CEST effect (26,50). Due to limited molecular motion, semi-solid protons are coupled strongly via through-space dipole–dipole coupling resulting in spin diffusion between all protons. As a consequence, the T_2 is extremely short, on the order of 10 μs for Agar (49) and 50–70 μs for brain tissues (51). Therefore, the semi-solid pool can be treated as a single proton ensemble or proton bath. The magnetization of this semi-solid pool can be transferred to the water pool via several pathways:

1. Dipolar coupling between bound water and the semi-solid component (pathway A in Fig. 1b (52,53)), which is on the order of 50–100 kHz (26) and causes fast magnetization exchange.
2. Chemical exchange (pathways B, C, and D in Fig. 1b (54)). Some studies suggest that this transfer actually is significant and comparable with the transfer by dipolar coupling if the semi-solid pool includes a large amount of exchangeable protons (26,55). The majority of the OH groups (hydroxyl) and NH_2 groups (amine, cytosine, and NH_3^+) exchange rapidly with a rate of more than 1 kHz (55), while the amide and $NHNH_2$ (guanidyl) protons generally exchange slower (<1 kHz).

Thus, the semi-solid component can be treated as a single spin pool with short T_2 but with an averaged exchange rate as determined by the above transfer pathways. For simplicity, we can classify the exchange rate by fast exchange processes, mainly from strong dipolar coupling and fast exchanging protons (OH groups and NH_2 groups), and slow/intermediate exchange process from amide protons and guanidyl ($NHNH_2$) groups (56). Note that fast and slow exchange rates are generally defined with respect to the NMR time scale, which depends on the chemical shift difference between the water and solute protons. The intermediate exchange rate thus applies to this study conducted at 11.7 T, but this could

become fast exchange for some pools at lower field strengths such as 3 T. The chemical shift range for the semi-solid pool spans more than 40 ppm (from −20 ppm to 20 ppm with respect to water) for rat brain. The center frequency of the semi-solid pool is determined by the proton density weighted chemical shift of all the protons in the solid pool, which is at the aliphatic frequency for tissues in vivo (36,57). It is caused by the large number of aliphatic protons in tissues as suggested in a recent study on Bovine myelin (51).

Compared to the semi-solid component, the dipolar coupling and NOEs between protons in mobile macromolecules are much weaker due to the relatively fast tumbling of the molecules. The major distinguishing characteristic of mobile protein/lipid components is the millisecond transverse relaxation time (49) of their protons, which can therefore be treated as separate groups, that is spectroscopically distinct species. While the magnetization can still transfer via dipolar coupling and NOE crossrelaxation, the magnitude and sign are strongly dependent on molecular dynamics, which is affected by molecular size, viscosity, and binding. The magnetization of the nonexchangeable aliphatic/olefinic and aromatic protons (pathways H and I in Fig. 1b) can still exchange with water via a two-step process. First, magnetization is transferred from non-exchangeable to exchangeable protons via NOE cross-relaxation and intramolecular dipolar coupling, followed by chemical exchange to water. The strength of the direct dipolar coupling between aliphatic/olefinic/aromatic protons and water is determined by the mobility of the macromolecules and water bound to it. While such direct coupling contributes significantly to the conventional MTC, this interaction has been shown to be negligible relative to amide proton exchange in mobile proteins (26,42,45). For intermediate size molecules such as glycosaminoglycan and cartilage, the direct NOE/dipolar coupling will be more significant and may become comparable and even higher than the rNOE depending on the range of motion and strength of water binding. In addition to rNOE-CEST transfer, chemical exchange of directly saturated exchangeable protons contributes to water saturation in mobile species. In conventional APT experiments, the signal is from the relatively slow chemical exchange (10–30 Hz (26)) from the amide protons (pathway E in Fig. 1b). Other proton groups such as the NH_2 and OH groups (pathways F and G in Fig. 1b), which have exchange rates in the range of 700–10,000 Hz (55), contribute only when using very high RF power to saturate them partially before exchange or very long t_{sat} so that very small amounts of saturation can accumulate to become significant.

Pulse Sequence—The VDMP-CEST sequence is illustrated in Figure 1a. It is similar to the conventional pulsed MTC sequence (54,58,59) with a CYCLOPS (CYClically Ordered Phase Sequence) type phase cycle within each block of four 180° pulses. The phase cycle and gradients are applied to destroy residual transverse magnetization (i.e., due to incorrect flip angle and further stimulated echoes) and we only consider longitudinal magnetization transfer. The VDMP-CEST sequence can be used as a T_2 filter and magnetization transfer rate filter to distinguish between the signals originating in each of the transfer pathways mentioned above.

T_2-filter: Due to the different relaxation properties of the proton pools involved, the RF pulses applied in VDMP-CEST affect them differently. The transverse relaxation time

constant, T_2, for semi-solid tissue components (49,60,61) and larger mobile proteins is short compared to the pulse width (~7 ms here) applied in the VDMP-CEST. For these, the selective pulses applied at the frequency offsets of these systems need to be treated as partial saturation instead of inversion. For highly mobile proton groups in proteins or protons in small peptides or metabolites, T_2 values are much longer than the pulses applied in VDMP-CEST and the pulses will cause frequency-selective inversion and not appreciably affect the water protons. A RF pulse bandwidth of 200–600 Hz (pulse width 6.9–2.3 ms) was used in this study, while the offsets used for amide and aliphatic protons were ±1800 Hz (±3.6 ppm) with respect to the water peak. When using selective inversion, the highest CEST signal will be achieved, namely twice as much as saturation or 90-excite followed by dephasing (2). The saturation efficiency is described in terms of the absorption lineshape of the protons and the saturation pulse power level v^2. For the continuous wave situation, the saturation efficiency is (62,63).

$$\lambda = \pi\omega_1^2 g(2\pi\Delta\Omega) \quad [1]$$

where $\Delta\Omega$ is the frequency offset. The absorption line shape, g, is a function of the transverse relaxation time constant of the system, and the integral of the lineshape function is equal to unity. The lineshape of the absorption function has been reported as Gaussian for Agar and Super-Lorentzian for semi-solid biological tissues (51,64). The Super-Lorentzian function is defined as:

$$g(\Delta\Omega T_2) = \sqrt{\frac{2}{\pi}} \int_0^{\pi/2} \frac{T_2 \sin\theta}{|3\cos^2\theta - 1|} \exp\left(-2\left[\frac{2\pi\Delta\Omega T_2}{3\cos^2\theta - 1}\right]^2\right) d\theta \quad [2]$$

with the difference between the Super-Lorentzian and Gaussian functions being that all tissue orientations with respect to the B_0 field are integrated. The exact absorption lineshapes for the system with different effective T_2 values has been calculated in the literature (59). Whether a Gaussian or Super-Lorentzian function is applied, it can be seen that the saturation efficiency on resonance, i.e. at $\Delta\Omega = 0$, is linearly proportional to the effective T_2. Then, the saturation efficiency of the semi-solid pool will be several hundred times smaller than the mobile protein/lipid pool for the on resonance situation as seen from their T_2 ratio. Consequently, the saturation pulse can be used as a T_2 filter to separate the CEST effect from the MTC effect if low-power pulses are applied (41,49). It is worth noting that the T_2 value in Eq. [2] is an effective one, $T_{2,\text{eff}}$. Therefore, for the water exchangeable protons, $T_{2,\text{eff}}$ is described by $1/T_{2,\text{eff}} = k + 1/T_2$, where k is the exchange rate. A similar conclusion can be reached from the Bloch equations (2,6,65). The absorption lineshape of the free water pool is Lorentzian. In our pulsed CEST sequence, the pulse amplitudes are shaped. Deriving an exact analytical solution for the magnetization of the semisolid pool for a train of shaped pulses is non-trivial. However, approximate solutions for MTC have been derived for equivalent area rectangular pulses by Sled and Pike (54), Ramani et al. (66), and Yarnykh (61). In the current article, the exchange process was simulated by numerically solving the Bloch equations (65,67) without applying the above approximations, that is simulating the saturation effect of the Gaussian pulses. In the Bloch simulation, the Gaussian

shaped pulses were approximated by 256 narrow rectangular pulses. The saturation power indicated in the work is the peak power of the Gaussian pulses.

In tissues, there is a broad distribution of T_2's due to different molecular sizes and concomitant mobilities of the protons in the proteins/lipids, ranging from 0.008 ms to 26 ms in myelin lipids (51,68) and probably up to 100 ms in more mobile peptides and metabolites. When varying the power of the pulses applied in VDMP-CEST, protons with different T_2 values will experience different saturations, which is illustrated in Figure 2. It needs to be mentioned that the line broadening effect induced by the direct saturation of the pulses is neglected in this simulation. For weak pulses, only the mobile proteins are saturated and the amide and aliphatic/olefinic proton peaks will be spectroscopically distinguishable at offsets of about ±3.6 ppm respectively, which is the case observed in CEST experiments. With increased saturation power, more and more proteins/lipid protons with short T_2 values will be saturated, which causes the two proton groups (amide and aliphatic/olefinic) to start overlapping. Eventually, the two groups will merge into a single broad peak at strong power, which is the case observed in conventional MTC experiments. From this simulation, it can be seen that the VDMP-CEST approach can target different proton groups, in contrast to the MTC experiment. To accomplish this, the saturation power has to be low enough to avoid overlap of the proton groups, but sufficiently high for measurable effects. In the current study, we found that 4 μT (200 Hz bandwidth) Gaussian pulses were a proper choice at 11.7 T, allowing separation of APT signal from rNOE-CEST, while still maintaining reasonable signal to noise ratio. The simulation also explains the observation by others that a strong rNOE-CEST is observed for lower power (<2 μT) continuous wave saturation CEST pulses, while the rNOE-CEST will disappear at strong saturation power due to the dominance of the aliphatic/olefinic peaks of semisolid protons (39).

Magnetization transfer rate filter: Under the assumption of a two-pool exchange model, the magnetization transfer process, that is the VDMP SI curve, observed for a pulsed MT/CEST sequence will show two phases in time, namely saturation buildup and subsequent decay with T_1 of water (T_{1w}) (69) and, for high concentration of protons, due to the back exchange process (25,70). The peak time point (t_{peak}), that is the time at which the saturation level peaks, depends upon the relative rate constants of transfer and relaxation. For very fast transfer, the magnetization exchange already occurs during the pulse time (t_p). The buildup/decay process for a VDMP-CEST sequence resembles the situation when using label transfer modules, similar to the frequency-labeled exchange sequence (71). In the VDMP-CEST, the pulse performs the labeling while transfer occurs during the mixing time (t_{mix}). Therefore, an analytical equation can be used to describe the proton transfer ratio under the assumption that the combined label and transfer period ($t_p + t_{mix}$) is much smaller than T_{1w} and the exchange rate (k) is slow enough for exchange during the pulses (t_p) to be neglected.

$$PTR = X \cdot \lambda \cdot \eta \cdot \beta \quad [3a]$$

$$\eta = \sum_{i=1}^{n} e^{-n t_{\mathrm{mix}}/T_{1\mathrm{w}}} \quad [3b]$$

$$\beta = 1 - e^{-K \cdot t_{\mathrm{mix}}} \quad [3c]$$

where X is the concentration ratio between exchangeable and water protons, λ is the saturation efficiency (Eq. [1]), and β the exchange transfer efficiency. The proton transfer ratio is further determined by the sum of the magnetization transferred by the n pulses. In the equation, the efficiency factor β describes the buildup process and is effectively an exchange filter (2,71). Equation [3a] is useful to understand the idea of saturation buildup with k and decay with $T_{1\mathrm{w}}$, and illustrates how the sequence is an exchange filter. However, for the long pulse widths used here (3–7 ms) in VDMP-CEST, Eq. [3a] will be suitable only for extremely slow exchange processes. To be exact for the wide range of exchange rates covered here, we therefore simulated the exchange process by numerically solving the Bloch equations for two pools, one exchangeable proton pool and the free water pool. A detailed description of the procedure has been published elsewhere (65,67).

In the two-pool model, the decay process is a function of $T_{1\mathrm{w}}$ and the back exchange rate (Eq. 3b). The apparent decay rate with respect to the mixing time is determined by $n/T_{1\mathrm{w}}$ (Eq. 3b). Therefore, the decay will be faster when a larger number of pulses is applied, which is due to the fact that total preparation period, that is $n \times (t_{\mathrm{p}} + t_{\mathrm{mix}})$, will be longer. The decay caused by $T_{1\mathrm{w}}$ relaxation and back exchange process is accounted for in the two-pool Bloch simulation. Besides the $T_{1\mathrm{w}}$ relaxation and back exchange induced decay, additional sources of saturation decay will occur in vivo due to interference from other transfer effects such as from MTC and rapidly exchanging amine protons, which are commonly seen in proteins and tissues. Here we term interference of such processes as saturation cross-transfer (SCT). In the cross-transfer process, magnetization from the semisolid and other solute pools that is transferred to the bulk free water pool is subsequently transferred to the solute proton pool under study (and not necessarily back to the original pool). Considering the large MTC pool, this cross-transfer process is far more significant than the back exchange process for the small solute pool under study. For the rNOE-CEST, the main source of cross-transfer comes from the MTC pool but SCT from amine and hydroxyl protons will also contribute to the APT-CEST signal. Therefore, the decay of the VDMP SI curve at the APT-CEST resonance frequency is usually much faster than that at the rNOE-CEST frequency. In principle, SCT may also contribute to the saturation buildup curve. However, the MTC and fast exchanging protons were considered as fully exchanged during the pulses used in this study and therefore only the decay process of the SCT was considered. A sophisticated three-pool model, that is water pool, solute proton pool, and MTC pool should be able to explain the observed decay curves in tissues more precisely. However, this is beyond the scope of this article and an effective $T_{1\mathrm{w}}$ $(T^{*}_{1\mathrm{w}})$ was used in the simulation to describe the faster decay due to the cross-transfer processes.

The above theory suggests that APT and rNOE-CEST can be separated from MTC and other effects when combining proper pulse powers (T_2 filter) and pulse delays (magnetization

transfer rate filter) in VDMP-CEST. The proposed fast method for APT and rNOE-CEST MRI in the current work consists of recording two images with two pulse delays, one with zero mixing time and another at the mixing time where the maximum APT-CEST or rNOE-CEST saturation is reached, that is t_{peak}. Then, the APT or rNOE aliphatic CEST can be obtained by subtracting the two images. However, the zero mixing time could not be reached experimentally due to the spoiler gradient after the pulses. Instead, the minimum mixing time was used in our experiments. By using a low pulse power and fewer RF pulses in the train, semisolid protons and very rapidly exchanging protons will be only weakly saturated (see Fig. 2). When subtracting the two images these two contributions will reduce even more (close to negligible) and the direct water saturation will be removed. An APT image obtained this way (irradiation at 3.6 ppm and varying the delay) is therefore expected to be free of interference from MTC asymmetry, amine and hydroxyl proton contributions and, since no asymmetry analysis is done, from rNOEs from aliphatic protons. Therefore, we name it clean-APT to distinguish it from the traditional APT-weighted method based on MTR_{asym} determination.

MRI

MRI experiments were performed on a horizontal 11.7 T Bruker Biospec system equipped with actively shielded gradients of maximum strength 74 Gauss/cm. Experiments on phantoms were performed using a 23 mm volume transceiver coil (Bruker, Germany) at room temperature. The image acquisition was achieved using a fast spin-echo sequence with TR/TE =13 s/4 ms, NA = 1, 50 kHz receive bandwidth, slice thickness 1 mm, and 32 × 32 image matrix (field of view (FOV) 2 × 2 cm^2). In the VDMP-CEST sequence, depending on the application, 4–64 Gaussian shaped RF pulses (180 degree flip angle) were applied during preparation. Pulse powers of 4 μT (6.9 ms, 200 Hz bandwidth) and 12 μT (2.3 ms, 600 Hz bandwidth) were used. A Z-spectrum was recorded from −7 ppm to 7 ppm in steps of 0.4 ppm. An S_0 image was recorded by setting the irradiation offset to 200 ppm.

For the rat study, a 72 mm quadrature volume resonator (Bruker, Germany) was used for transmission and a 2 × 2 phased array coil (Bruker, Germany) for reception. CEST images were acquired using a fast spin-echo readout with TR/TE = 6 s/4 ms, NA = 1, slice thickness 1 mm, and 64 × 64 matrix (FOV 1.8 × 1.8 cm^2); eight Gaussian shaped RF pulses (180 degree flip angle) with peak powers ranging from 2 μT (t_{pulse} = 13.8 ms) to 12 μT (t_{pulse} = 2.3 ms) were used for recording the VDMP-CEST images. The Z-spectrum was recorded from −20 ppm to 20 ppm. The proper pulse delay t_{mix} and the number of saturation pulses was selected by acquiring the water saturation as a function of delay time and determining the equilibrium point between transfer buildup and relaxation decay. The B_0 field over the rat brain was adjusted using field mapping and second order shimming. The quality of the shim was examined using the water saturation shift referencing method.

Sample Preparation

Three samples representing different mobility molecules in tissues were used to demonstrate the VDMP-CEST sequence. Mobile proteins in tissue were mimicked by BSA (66.5 kDa, Sigma Aldrich, St. Louis A2058) solution (10% by weight; 1.5 mM; pH = 7.3) in a 5 mm NMR tube. Semi-solid proteins in tissue were modeled using a crosslinked 10% BSA

sample at pH 7.3. Crosslinking was achieved by heating the solution in a 80–90°C water bath for 30 min after which a transparent gel-like sample was formed. The crosslinked BSA sample showed strong dipolar coupling similar to the traditional MTC phantom (agar).

A Glu solution was used to model small metabolites in tissue, particularly the amine group, the exchange of which competes with the amide protons and the chemical shift range of which overlaps due to exchange broadening. A 12.5 mM Glu (Sigma Aldrich, St. Louis, G1251) solution was prepared in phosphate buffered saline (PBS) to pH = 7.3. The chemical shift and exchange rate (at physiological pH and temperature) of the amine proton were previously reported to be 3 ppm and 5500 Hz, respectively (11). The conventional Z-spectrum of Glu therefore shows a broad saturation signal for which the center frequency cannot be clearly assigned. Also, the temperature was different here, which may change the shift, and the VDMP scheme is not able to measure high exchange rates reliably. For simplicity, we therefore used values of 2.5 ppm and 6000 Hz for the fitting of VDMP SI curves of amine protons.

In Vivo Studies

The study was approved by the institutional animal care and use committee. Five adult male Wistar rats weighing 280–320 g were anesthetized using 5% isoflurane in a 75%/25% air/oxygen mixture, followed by 2–2.5% isoflurane during the MRI scan. The rat head was immobilized by a bite bar and two ear bars. During scanning, rats were placed on a water heated animal bed equipped with temperature and respiratory control. Respiration was monitored and maintained at 20–30/min. After the scans, the anesthetized rats were sacrificed by injection of saturated KCl. Of the five rats, three were used to record the full Z-spectrum and VDMP SI curves using the VDMP sequence, while the other two were used to perform high-resolution APT-CEST and NOE-CEST images. The results from all rats were very reproducible.

Data Analysis

The VDMP SI curves of the phantoms and rat brain were fit with a two-pool Bloch model. The fitting parameters were the effective T_1 of water (T^*_{1w}), exchangeable proton fraction with respect to water proton concentration (X), exchange rate (k), and one constant contribution due to direct water saturation (DS). DS varies with frequency offset, but is a constant value with respect to the mixing time at a particular frequency offset. T_2 values for the water pool (T_{2w}) of phantoms were determined by Carr-Purcell-Meiboom-Gill (CPMG) experiments (T_{2w} = 110 ms, 108 ms and 78 ms for Glu, BSA solution, and crosslinked BSA, respectively), while the T_{2w} of rat brain was set to 36 ms based on the literature (72). T_2 and T_1 for the exchangeable solute pool (T_{2s} and T_{1s}) were difficult to measure experimentally and we therefore used typical literature values (listed in the figure captions). In the fitting, however, it was found that the exchange rates and the shape of VDMP SI curves were not sensitive to the values of T_{2w} and T_{2s}, thus allowing the proper determination of exchange rates from fitting these curves even with uncertainty regarding precise T_{2s} values. The T_{2s} value of the crosslinked BSA could also be determined from lineshape fitting of the VDMP difference spectrum. Therefore, the VDMP SI curves of crosslinked BSA phantom were fitted using the experimentally determined T_{2s}. The maximum saturation level in VDMP SI

curves is determined by the exchangeable proton fraction x. However, unlike the exchange rate, the accuracy of x is significantly affected by the uncertainty of the T_{2w} and T_{2s}, since the saturation efficiency is related to the T_{2s} as seen from Eq. [1]. In the fitting, the back exchange process is automatically accounted for in the Bloch equations (see simulation in Fig. 3b). The T_{1w}^{*} values are smaller than T_{1w} mainly due to the cross-transfer processes discussed above. The interference will be more obvious for higher pulse numbers or when a large MTC pool is present, as seen in the fitting on rat brain (Fig. 7).

Results

Simulations

In Figure 3, the results of Bloch simulations for 70 mM amide protons in water (amide proton fraction 6.36×10^{-4}) are shown for the VDMP-CEST sequence of Figure 1a using B_1 = 4 μT and t_{pulse}= 6.9 ms (200 Hz bandwidth). Figure 3a shows Z-spectra when using eight pulses and mixing times of 0 ms and 110 ms for an exchange rate of 20 Hz. The VDMP difference spectrum around 3.6 ppm shows only the amide proton peak and is a clean-APT spectrum. The direct water saturation effect due to the Gaussian pulses is canceled out at this frequency, because it is determined by the pulse length and strength and not the inter pulse delays that are short with respect to T_{1w}. Figure 3b shows the VDMP SI curves as a function of mixing time for exchange rates ranging from 50 Hz to 5000 Hz. For the very rapidly exchanging protons, the saturation already reaches equilibrium during the saturation pulses, that is for inter-pulse delays of zero, which is expected to be the case for most amine and hydroxyl protons. Therefore, varying the mixing time will not increase the CEST signal for such fast exchanging protons if the water relaxation time is sufficiently long. When eight pulses are applied, the water saturation at t_{peak} for slowly exchanging amide protons (k = 20 Hz) is still small (a few percent) and t_{peak} is reached at longer mixing time (110 ms). Therefore, the inter-pulse delay time, t_{mix}, can be used as a filter for different exchange rates. The effect of number of saturation pulses is simulated in Figure 3c. When the number of pulses is very high, t_{peak} reduces due to a much quicker decay because of a longer predelay. On the other hand, a low pulse number will lead to less CEST signal enhancement. The selection of the proper pulse number is thus a balance between these. In order to test whether B_1 inhomogeneity affects the VDMP SI curves, we simulated such curves for B_1 = 4 μT with a 0.5 μT error. The curves are similar with offsets due to the direct water saturation effect at different saturation power. The VDMP differences show that the sequence has some B_1 dependency.

Glutamic Acid Solution

Figure 4 shows Z-spectra for the 12.5 mM Glu solution recorded using an 8-pulse (a,b) and 32 pulse (d,e) VDMP-CEST sequence with B_1 = 4 μT (d) or 12 μT (e). The Z-spectrum recorded using conventional CEST is plotted in Figure 4c for comparison. The VDMP Z-spectrum recorded with 8-pulses was identical to one recorded on PBS (data not shown). It can be seen that amine protons with fast exchange rates cannot be observed with such a low pulse number and power, even at long mixing time (Fig. 4b). Under these experimental conditions, the interference from amine protons would be removed completely when recording APT images. When increasing the number of pulses to 32, a small effect becomes

visible at 4 μT (Fig. 4d) and when increasing B_1 to 12 μT (Fig. 4e) a clear mixing time dependence becomes visible, but this is a decay contrary to a buildup, similar to the simulation results (Fig. 3b) when comparing fast versus slowly exchanging protons.

Bovine Serum Albumin Studies

The VDMP SI curves for the BSA solution and crosslinked BSA at offsets of 3.6 ppm and −3.6 ppm using 8 pulses of 4 μT power are plotted in Figure 5a,b, respectively. The solid lines are the curves fitted using the two-pool Bloch equations with T_{1s} and T_{2s} assumed as indicated in the figure legend. The amide proton exchange rate (k^{NH}) of the BSA solution at room temperature was found to be 13 Hz, while the aliphatic magnetization transfer rate (k^{rNOE}) was only 3 Hz. Once the BSA protein was crosslinked (Fig. 5b), the VDMP SI curves at both −3.6 ppm and 3.6 ppm changed significantly compared to the BSA solution in that the curve shapes became similar for the amide and aliphatic offsets, as reflected in the rates k^{NH} = 60 Hz and k^{rNOE} = 50 Hz. This confirms that the crosslinked BSA can be treated as a single proton pool with an exchange rate that is similar for each offset and amounts to the average from all exchange processes, including dipolar coupling and proton exchange. The effect of peak saturation power (note that bandwidth varies as pulses are always 180°) on the amide proton pool (BSA-APT) and MTC pool (crosslinked BSA) is demonstrated in Figure 5c for an 8-pulse sequence. Here the signal at offset −7 ppm was used to study MTC in order to avoid potential interference from highly mobile side chain amide and aliphatic protons in crosslinked BSA. The VDMP saturation difference signals for both MTC and BSA-APT signals were proportional to the saturation power. For these experimental conditions, a saturation power lower than 4 μT would be sufficient to suppress the MTC interference.

In Figure 6, 8-pulse VDMP-CEST data for BSA solution (Fig. 6a,b) and crosslinked gel (Fig. 6c,d) are shown for B_1-levels of 12 μT (Fig. 6a,c) and 4 μT (Fig. 6b,d). Each dataset shows Z-spectra recorded at two mixing times (bottom) and the corresponding VDMP difference spectrum (top). At the minimum 0.7 ms mixing time in solution, there is only a very small saturation effect in the upfield region in the Z-spectrum, i.e. the aliphatic proton range, while there is already a broad saturation dip downfield (around 2–5 ppm) attributed to the rapidly exchanging amine protons centered around 2.2 ppm when in the intermediate exchange regime (15). This strong saturation of the amine protons will complicate clean detection of the amide protons when using traditional asymmetry analysis. With the variable delay approach, however, the two proton types can be separated based on their significantly different exchange rates (Fig. 6a,b). As demonstrated in the simulations (Fig. 3b) and the Glu experiments (Fig. 4), the CEST effect from rapidly exchanging protons does not increase with mixing time since their transfer is already accomplished during the pulses. The VDMP-CEST difference spectra in Figure 6a,b therefore show effects mainly from slowly transferred saturation, such as for chemical exchange of amide protons at 3.6 ppm, and rNOEs for aliphatic protons in the upfield range. The integral of the aliphatic CEST signal is more than double the APT signal. The CEST spectrum at lower saturation power can be measured over a somewhat larger spectral range closer to water, due to the fact that less direct water saturation occurs. When 4 μT (200 Hz bandwidth) inversion pulses are used, the bandwidth is lower than for 12 μT (600 Hz bandwidth), resulting in weaker CEST and rNOE

effects. However, the VDMP difference spectrum recorded with 4 μT pulses has much higher spectral resolution (Fig. 6b).

For the crosslinked BSA sample, the Z-spectra and VDMP difference spectra differ significantly from those in solution. The amide proton dip (2–5 ppm) in the Z-spectrum is difficult to distinguish because the strong dipolar coupling among all protons leads to a broad solidlike spectrum. The VDMP difference spectrum is not as well defined as for solution, but broader due to the strongly coupled matrix. The T_2 of the crosslinked BSA protons was estimated by fitting the lineshape of the VDMP difference spectrum assuming pools from one aliphatic group and one amide group only. This resulted in a T_{2s} of 130 μs and the proton density ratio aliphatic:amide of 2.5:1. It is worth noting that this T_{2s} value reflects the averaged relaxation time of the protons saturated with peak power 12 μT. When using 4 μT pulses (Fig. 6d), the difference spectrum only shows a slight signal decrease in the exchangeable proton region downfield, which is due to the T_1 recovery of water during the mixing time (Fig. 3c). A small increase is still visible upfield, which may arise from side chains of the proteins with higher mobility. A comparison to the VDMP difference spectrum in BSA solution (Fig. 6b) suggests that a series of eight Gaussian inversion pulses of 4 μT strength should be able to separate the amide and amine protons in mobile proteins from the semi-solid pool, while the majority of any upfield effect should be from mobile proteins.

Animal Studies

The VDMP SI curves for rat brain cortex are plotted as a function of number of inversion pulses in Figure 7. The SI curves are similar to the simulation in Figure 3c. As expected, the APT/rNOE effect will be enhanced by more pulses, but the maximum enhancement is limited by T_{1w}, back exchange, and cross-transfer processes involving all saturated water protons (i.e., amides will have interference from MTC and amines). These SCT processes will cause quick decay of the VDMP SI curves, which can be seen from the mismatch between the simulated curves and the experimental data recorded with 16 pulses, where the interference of semisolid pool becomes significant. The experimental data recorded with low pulse numbers can be well explained by the Bloch simulation as seen from the fitting curves in Figure 7. Due to the extremely weak APT effect observed with four pulses VDMP sequence, the experimental data collected with four pulses are not fitted (Fig. 7a). From the VDMP SI curves, it can be seen that eight pulses is an excellent choice for B_1 = 2 μT, achieving enough enhancement of APT/rNOE while minimizing interference from MTC and other fast exchanging protons. For this number of pulses, the saturation reaches steady state at around 110 ms for aliphatic and amide protons and a difference effect similar to 16 pulses (Fig. 7c). When fitting all SI curves combined (multivariate), amide proton and rNOE exchange rates of 30 Hz and 17 Hz were found. Here, a saturation power of 2 μT was chosen to make sure that the interference from MTC and amine protons was fully suppressed. When performing a similar experiment for B_1 = 12 μT (600 Hz), the eight pulse sequence was also the optimized condition, reaching a maximum saturation at 110 ms for both amide and aliphatic protons (data not shown). This is consistent with the theory (see Eq. [3a]) in that t_{peak} is determined by the exchange rate and T_{1W} and not dependent on saturation power.

In Figure 8, VDMP-CEST spectra for healthy rat brain cortex acquired using saturation pulses of 12 μT and 2 μT are plotted for two mixing times. At 12.0 μT, the VDMP difference spectra illustrate the T_2 filter effect of the Gaussian saturation pulses. In the VDMP spectra recorded with low power pulses, the amide/aliphatic peaks are better resolved but have lower signal to noise (approximately five times lower).

APT and rNOE VDMP difference images of a rat brain acquired using 2 μT and 12 μT pulses are shown in Figure 9a,b and Figure 9d,e, respectively. The MT asymmetry images (MTR_{asym}) images obtained by the traditional asymmetry analysis are also plotted for comparison. At the lower peak power of 2 μT, the images at offsets 3.6 ppm (c) and −3.6 ppm (d) differ appreciably and most likely reflect clean-APT and rNOE-CEST effects. Both clean-APT and rNOE-CEST of muscle are significantly lower than the values of the brain.

Discussion

We introduced a VDMP CEST sequence consisting of a series of frequency-selective inversion pulses separated by inter-pulse delays that can be used to selectively detect slower magnetization transfer processes such as amide proton exchange and rNOEs. The pulse sequence can function as a T_2 filter by varying the B_1 strength of the pulses and as an magnetization transfer rate filter by varying the inter-pulse delay (mixing time) and the number of pulses. For the current field strength, a sequence with eight inversion pulses and B_1 of 4 μT was sufficient to predominantly detect APT and rNOE processes by performing a series of experiments at 0.7 ms and 110 ms delays. Phantom experiments on rapidly exchanging amine protons (Fig. 4) and protein solution and gel (Figs. 5–7) confirmed the theoretical simulations using a two-pool Bloch model (Fig. 3) in that effects of rapidly exchanging protons and direct water saturation can be subtracted out and that interference of MTC effects can be minimized.

We used a protein solution (1.5 mM BSA in buffer at pH = 7.3) and crosslinked gel of the same protein to approximate in vivo conditions for protons in mobile proteins and semi-solid protons, respectively. The experimental results in solution showed that the rNOE-CEST saturation buildup rate as a function of mixing time is slower than that of amide protons (Fig. 5a). The measured k^{NH} of 13 Hz represents an average at room temperature for all amide protons in BSA and is consistent with the typical literature range of 0–100 Hz (50,73). For each individual amide proton, the base-catalyzed exchange rate depends on the position in the secondary structure of the BSA protein and its water accessibility. The initial point of the time-dependent saturation curves in Figure 5a, in addition to some CEST, has contributions from direct water saturation, the fast exchanging protons, and the MTC effect. The abundant amine protons in BSA make the initial point of these curves higher at amide proton offset (3.6 ppm) than at the aliphatic offset (−3.6 ppm). The situation is quite different for the crosslinked protein (Fig. 5b), where the initial saturation is much larger and comparable in magnitude at both offsets. The reason is that the semi-solid matrix for this gel is strongly coupled and close to the ultimate limit of a single spin bath, for which the build up curves would also be equivalent. Here the shape and onset of the curves are comparable, while only a small difference in magnitude remains. This transition to a single spin bath is also reflected in the change of the k^{NH}/k^{rNOE} ratio from 4.3 in solution to 1.2 in the gel. A

large portion of saturation will exchange with water through intramolecular spin diffusion followed by either exchange relay via the amine protons (pathway C in Fig. 1b) or direct through-space dipolar coupling (Pathway A in Fig. 1b) already during the pulse and cause strong water saturation at the 0.7 ms mixing time (see Figs. 6c,d and 7b). As a consequence, the VDMP difference spectrum (Fig. 6c) for the gel is not as well defined as for solution, showing a broad spectrum similar to the dashed brown curve in Figure 2. As mentioned earlier, the mixing-time dependent VDMP intensity curve of the crosslinked BSA at any offset actually covers all possible exchange pathways due to the fast spin diffusion within the coupled system. Thus, the observed VDMP intensity curve at 3.6 ppm reflects not only the amide proton exchange rate, but also other slow and intermediate exchanging protons, many with exchange rates much higher than the average amide proton exchange rate in solution. Therefore, the measured exchange transfer rate k^{NH} in the gel is far higher than the amide exchange rate alone. Still, the extremely fast exchanging components from amine and dipolar coupling will probably not contribute much to the VDMP intensity mixing time dependence but mainly to the initial value of the curve.

The Z-spectra and VDMP difference spectra observed for rat brain are similar to the results recorded on BSA protein solutions. However, the protein size or mobility in rat brain covers a wide range. As a consequence, the VDMP difference spectra are not only affected by saturation efficiency, but also by molecular mobility similar to Figure 2. When using high power saturation pulses (12 μT), the difference spectra resemble a mixture of the crosslinked BSA and BSA solution with sharp amide and aliphatic peaks on top of a broad lineshape (Fig. 8b). Similar to the experiments on crosslinked BSA, the MTC effect could be reduced dramatically by using low power saturation pulses (see Fig. 8d), which is reflected in the different contrast pattern between Figure 9c and d, for which the VDMP difference spectrum for offsets further than ±10 ppm from water is already zero (Fig. 8d). Even though 4 μT saturation power already reduces the MTC and amine proton interference significantly, as shown in the BSA study, an even lower saturation power of 2 μT was applied to obtain spectra and images dominated by CEST signal from mobile proteins in brain tissue, and resemble the BSA solution study (Fig. 6b). In the applications of this technique, however, the saturation power does not necessarily need to be as low as 2 μT.

The clean-APT image recorded using 2 μT saturation pulses (Fig. 9d) does not show obvious contrast in the rat brain (note the reduced contrast scale). It indicates that the mobile protein concentration in the rat brain is quite uniform in the white matter and gray matter, which is consistent with a similar study on human brain by the pulsed-CEST technique (41,74). However, the rNOE-CEST not only has much higher signal compared to APT, it also shows obvious gray–white matter contrast. The white matter has higher rNOE-CEST signal. Although, the APT and rNOE-CEST images recorded with 12 μT pulses have much higher intensity compared to images recorded with 2 μT pulses, the amide proton and aliphatic proton peaks begin to overlap as shown from the VDMP difference spectra in Figures 2 and 8, and further evidenced from the image recorded at 3.6 ppm (Fig. 9a), where contrast similar to the rNOE-CEST (Fig. 9b) is observed. An APT image recorded using high power saturation pulses will be contaminated by other types of protons similar to traditional MTC images. The MT_{asym} images show the combined effect of both APT and NOE effects.

Technical Details

We have shown that the VDMP-CEST method provides an efficient and robust way of recording the APT and rNOE aliphatic/aromatic CEST effects. This technique shares many features with arterial spin labeling (ASL) (75) by taking the difference between a reference image and a labeled image. Recently, several new CEST techniques are being developed to remove the MT effect efficiently, including positive CEST (pCEST) (76), two frequency irradiation schemes (77), and Alternating-Phase Irradiation (ZAPI) (78) or to speed up the CEST acquisition, such as the length and offset varied saturation (LOVARS) (79), SAFARI (37), and CERT schemes (80). The VDMP-CEST has several favorable features. First, recording a full Z-spectrum is not necessary. Two or more images at one frequency offset and the proper pulse power and pulse delay can be recorded to give an APT or rNOE-CEST image (Fig. 9). Therefore, the VDMP-CEST images can be averaged multiple times at the same frequency to increase the signal to noise ratio. Secondly, in the VDMP-CEST method, the DS contribution is determined by the total pulse length and power. Thus an increase of the pulse delay will have no effect on DS, as confirmed by the VDMP results on the Glu and PBS solutions, in which the VDMP SI curves are constant when no interfering transfer processes are present and the offset is sufficiently far from water resonance (Figs. 4a,d and 6b,d). However, the DS cancellation will not be perfect when the water frequency is inadvertently affected by selective RF pulses, that is $\Delta <$ 600 Hz for 2.3 ms Gaussian pulses, due to the complicated nature of water transverse and longitudinal relaxation. Therefore, the VDMP-CEST difference image has negligible DS effects as long as the saturation offset is much larger than the bandwidth of saturation pulses. A third advantage is that the VDMP-CEST method is relatively insensitive to B_0 field inhomogeneities. In the conventional APT experiments, a B_0 field correction is required for the asymmetry analysis, since Z-spectra have a sharp dip around water offset induced by the water direct saturation. If the center of the Z-spectra is not shifted properly, the asymmetry analysis the Z-spectrum will give rise to strong artificial peaks that are an obstacle in obtaining the real APT signal. In VDMP-CEST, the difference spectrum of the two Z-spectra is quite broad around the amide and aliphatic protons. Consequently, a B_0 correction is not necessary and avoiding it further reduces the time for recording clean-APT and rNOE-CEST images.

A fourth significant advantage of the VDMP-CEST is that APT signal can be separated from the background signal from some fast exchanging (e.g., amine) protons. Part of the broadened amine NMR spectrum is in the same frequency range as amide protons. Also, most exchangeable protons in small metabolites are fast exchanging protons, and in the offset around 0–2 ppm. The conventional asymmetry analysis is not able to distinguish amide proton from fast exchanging protons, since all of them generate saturation dips in Z-spectrum. The VDMP-CEST can separate APT effects from other protons efficiently by their significantly different exchange rates as shown in the study on BSA solutions. However, there are still some exchangeable protons with intermediate exchange rates, such as for instance the guanidyl protons in creatine, whose exchange rates are in the order of several hundred Hz. The VDMP-CEST sequence will still detect these as seen from signal at 2 ppm in the VDMP difference spectra from BSA (Fig. 6b) and rat brain (Fig. 8d). The VDMP signal at 2 ppm is comparable to APT signal. At 11.7 T, the offset of APT (3.6 ppm) is sufficiently far from the guanidyl protons (2 ppm), and an APT-CEST image will be still

mainly from amide protons. However, interference may be an issue at 3 T, where the offset difference is much smaller in Hz. Therefore, NOE-CEST should be a more reliable way of detecting protein concentrations, since almost no exchangeable protons resonate in the upfield region of the spectrum.

Several of the above mentioned advantages of VDMP sequence are also available in the recently proposed CERT scheme (47), which acquires two images with different flip angles on amide protons while maintaining the same pulse power at the same offset. However, the proposed VDMP scheme has several additional advantageous features. First, the CERT method requires careful calibration of pulse power to ensure that the two images are acquired with exactly same power and with flip angles of 180° and 360° for the amide protons. The VDMP is more flexible. Even though a 180° Gaussian pulse is suggested in the current VDMP study, other flip angles, pulse shapes, and saturation powers should also work. Second, in CERT, a train of pulses is applied similar to the pulsed-CEST sequence. In VDMP-CEST experiments, however, only a small number of Gaussian RF pulses need to be applied before image acquisition. Consequently, SAR and RF duty cycle limitations are avoided, which are a concern for experiments on human scanners. Also, the use of a small number of pulses has an extra advantage in that the VDMP-CEST is not very sensitive to the B_1 inhomogeneity, as shown in the simulations (Fig. 3d).

The technology can be translated to human studies, but some adjustments will be needed. In a 3 T scanner, the amide and aliphatic protons are at an offset of about 460 Hz with respect to water frequency (1800 Hz at 11.7 T). Thus, a much narrower bandwidth is needed to minimize water excitation. Thus, longer pulses are required, leading to more magnetization transfer due to the amide chemical exchange during the pulses and an attenuation of the VDMP difference signal. Another disadvantage at lower field magnet is the shorter T_{1w}, but since we are using a limited number of pulse-delay segments, this is not expected to be a major concern. However, the reduction in APT/rNOE signals due to above limitations can be compensated by averaging at one saturation frequency, which is a great advantage over conventional APT and rNOE CEST by asymmetric analysis.

Conclusion

We have developed a new method for rapidly measuring APT and rNOE-CEST effects by eliminating the process of recording a full Z-spectrum. The new method efficiently suppresses direct water saturation and the interfering effects of MTC and fast exchange protons efficiently by combining the proper pulse delay and pulse power in the VDMP-CEST sequence. The magnitude of the rNOE-CEST is several times higher than the APT effect. In addition to being a promising technique for obtaining APT and rNOE aliphatic CEST contrast, VDMP-CEST was also able to provide some insight into the mechanisms of MTC and CEST effects in tissue.

Acknowledgments

Authors thank Drs. Jinyuan Zhou, Guanshu Liu and Xiaolei Song for helpful discussions.

Grant sponsor: NIH; Grant numbers: R01EB015032, P50CA103175, R01EB015031, R01CA166171, R01EB009731, 1S10 RR028955, P41 EB015909.

References

1. Ward KM, Aletras AH, Balaban RS. A new class of contrast agents for MRI based on proton chemical exchange dependent saturation transfer (CEST). J Magn Reson. 2000; 143:79–87. [PubMed: 10698648]
2. van Zijl PCM, Yadav NN. Chemical exchange saturation transfer (CEST): what is in a name and what isn't? Magn Reson Med. 2011; 65:927–948. [PubMed: 21337419]
3. Zhou J, Zijl PCMv. Chemical exchange saturation transfer imaging and spectroscopy. Prog Nuclear Magn Reson Spectrosc. 2006; 48:109–136.
4. Sherry AD, Woods M. Chemical exchange saturation transfer contrast agents for magnetic resonance imaging. Annu Rev Biomed Eng. 2008; 10:391–411. [PubMed: 18647117]
5. Aime S, Castelli DD, Crich SG, Gianolio E, Terreno E. Pushing the sensitivity envelope of lanthanide-based magnetic resonance imaging (MRI) contrast agents for molecular imaging applications. Acc Chem Res. 2009; 42:822–831. [PubMed: 19534516]
6. McMahon MT, Gilad AA, Zhou J, Sun PZ, Bulte JWM, van Zijl PCM. Quantifying exchange rates in chemical exchange saturation transfer agents using the saturation time and saturation power dependencies of the magnetization transfer effect on the magnetic resonance imaging signal (QUEST and QUESP): Ph calibration for poly-l-lysine and a starburst dendrimer. Magn Reson Med. 2006; 55:836–847. [PubMed: 16506187]
7. Ling W, Regatte RR, Navon G, Jerschow A. Assessment of glycosaminoglycan concentration in vivo by chemical exchange-dependent saturation transfer (gagCEST). Proc Natl Acad Sci USA. 2008; 105:2266–2270. [PubMed: 18268341]
8. van Zijl PC, Jones CK, Ren J, Malloy CR, Sherry AD. MRI detection of glycogen in vivo by using chemical exchange saturation transfer imaging (glycoCEST). Proc Natl Acad Sci USA. 2007; 104:4359–4364. [PubMed: 17360529]
9. Chan KWY, McMahon MT, Kato Y, Liu GS, Bulte JWM, Bhujwalla ZM, Artemov D, van Zijl PCM. Natural d-glucose as a biodegradable MRI contrast agent for detecting cancer. Magn Reson Med. 2012; 68:1764–1773. [PubMed: 23074027]
10. Walker-Samuel, S.; Ramasawmy, R.; Torrealdea, F., et al. Quantitative imaging of tumour glucose uptake using glucoseCEST: comparison with 18F-FDG autoradiography; In Proceedings of the 20th Annual Meeting of ISMRM; Melbourne, Australia. 2012. p. 182
11. Cai K, Haris M, Singh A, Kogan F, Greenberg JH, Hariharan H, Detre JA, Reddy R. Magnetic resonance imaging of glutamate. Nat Med. 2012; 18:302–306. [PubMed: 22270722]
12. Zhou J, Lal B, Wilson DA, Laterra J, van Zijl PCM. Amide proton transfer (APT) contrast for imaging of brain tumors. Magn Reson Med. 2003; 50:1120–1126. [PubMed: 14648559]
13. Gilad AA, McMahon MT, Walczak P, Winnard PT Jr, Raman V, van Laarhoven HW, Skoglund CM, Bulte JW, van Zijl PC. Artificial reporter gene providing MRI contrast based on proton exchange. Nat Biotechnol. 2007; 25:217–219. [PubMed: 17259977]
14. McMahon MT, Gilad AA, DeLiso MA, Cromer Berman SM, Bulte JWM, van Zijl PCM. New "multicolor" polypeptide diamagnetic chemical exchange saturation transfer (DIACEST) contrast agents for MRI. Magn Reson Med. 2008; 60:803–812. [PubMed: 18816830]
15. Jin T, Wang P, Zong X, Kim SG. Magnetic resonance imaging of the Amine–Proton EXchange (APEX) dependent contrast. NeuroImage. 2012; 59:1218–1227. [PubMed: 21871570]
16. Woods M, Woessner DE, Sherry AD. Paramagnetic lanthanide complexes as PARACEST agents for medical imaging. Chem Soc Rev. 2006; 35:500–511. [PubMed: 16729144]
17. Zhang S, Merritt M, Woessner DE, Lenkinski RE, Sherry AD. PARACEST agents: modulating MRI contrast via water proton exchange. Acc Chem Res. 2003; 36:783–790. [PubMed: 14567712]
18. Angelovski G, Chauvin T, Pohmann R, Logothetis NK, Toth E. Calcium-responsive paramagnetic CEST agents. Bioorg Med Chem. 2011; 19:1097–1105. [PubMed: 20691598]

19. Shah T, Lu L, Dell KM, Pagel MD, Griswold MA, Flask CA. CESTFISP: a novel technique for rapid chemical exchange saturation transfer MRI at 7 T. Magn Reson Med. 2011; 65:432–437. [PubMed: 20939092]
20. Liu G, Moake M, Har-el Ye, et al. In vivo multicolor molecular MR imaging using diamagnetic chemical exchange saturation transfer liposomes. Magn Reson Med. 2012; 67:1106–1113. [PubMed: 22392814]
21. Cai K, Kiefer GE, Caruthers SD, Wickline SA, Lanza GM, Winter PM. Quantification of water exchange kinetics for targeted PARACEST perfluorocarbon nanoparticles. NMR Biomed. 2012; 25:279–285. [PubMed: 21751273]
22. Flament J, Geffroy F, Medina C, et al. In vivo CEST MR imaging of U87 mice brain tumor angiogenesis using targeted LipoCEST contrast agent at 7 T. Magn Reson Med. 2013; 69:179–87. [PubMed: 22378016]
23. Terreno E, Boffa C, Menchise V, Fedeli F, Carrera C, Castelli DD, Digilio G, Aime S. Gadolinium-doped LipoCEST agents: a potential novel class of dual 1H-MRI probes. Chem Commun (Camb). 2011; 47:4667–4669. [PubMed: 21409237]
24. Zhou J, Blakeley JO, Hua J, Kim M, Laterra J, Pomper MG, van Zijl PC. Practical data acquisition method for human brain tumor amide proton transfer (APT) imaging. Magn Reson Med. 2008; 60:842–849. [PubMed: 18816868]
25. Zhou J, Wilson DA, Sun PZ, Klaus JA, Van Zijl PC. Quantitative description of proton exchange processes between water and endogenous and exogenous agents for WEX, CEST, and APT experiments. Magn Reson Med. 2004; 51:945–952. [PubMed: 15122676]
26. van Zijl PCM, Zhou J, Mori N, Payen JF, Wilson D, Mori S. Mechanism of magnetization transfer during on-resonance water saturation. A new approach to detect mobile proteins, peptides, and lipids. Magn Reson Med. 2003; 49:440–449. [PubMed: 12594746]
27. Sun PZ, Zhou J, Huang J, van Zijl P. Simplified quantitative description of amide proton transfer (APT) imaging during acute ischemia. Magn Reson Med. 2007; 57:405–410. [PubMed: 17260362]
28. Osamu, T.; Takashi, Y.; Jochen, K.; Akio, H.; Koji, Y.; Kazufumi, K.; Yuriko, S.; Koji, S.; Masaya, T.; Hiroshi, H. Effect of saturation pulse length on parallel transmission based amide proton transfer (APT) imaging of different brain tumor types; In Proceedings of the 20th Annual Meeting of ISMRM; Melbourne, Australia. 2012. p. 0744
29. Jia G, Abaza R, Williams JD, et al. Amide proton transfer MR imaging of prostate cancer: a preliminary study. J Magn Reson Imaging. 2011; 33:647–654. [PubMed: 21563248]
30. Dula AN, Arlinghaus LR, Dortch RD, Dewey BE, Whisenant JG, Ayers GD, Yankeelov TE, Smith SA. Amide proton transfer imaging of the breast at 3 T: establishing reproducibility and possible feasibility assessing chemotherapy response. Magn Reson Med. 201210.1002/mrm.24450
31. Huang, AJ.; Jones, C.; Leigh, R.; Jarso, S.; Zijl, Pv. Initial application of PH-weighted imaging with pulsed CEST to image an acute ischemic stroke patient; In Proceedings of the 20th Annual Meeting of ISMRM; Melbourne, Australia. 2012. p. 1007
32. Sun PZ, Zhou J, Sun W, Huang J, van Zijl PCM. Detection of the ischemic penumbra using pH-weighted MRI. J Cereb Blood Flow Metab. 2006; 27:1129–1136. [PubMed: 17133226]
33. Zhou J, van Zijl PC. Defining an acidosis-based ischemic penumbra from pH-weighted MRI. Transl Stroke Res. 2011; 3:76–83. [PubMed: 22408691]
34. Sun PZ, Benner T, Kumar A, Sorensen AG. Investigation of optimizing and translating pH-sensitive pulsed-chemical exchange saturation transfer (CEST) imaging to a 3T clinical scanner. Magn Reson Med. 2008; 60:834–841. [PubMed: 18816867]
35. Pekar J, Jezzard P, Roberts DA, Leigh JS Jr, Frank JA, McLaughlin AC. Perfusion imaging with compensation for asymmetric magnetization transfer effects. Magn Reson Med. 1996; 35:70–79. [PubMed: 8771024]
36. Hua J, Jones CK, Blakeley J, Smith SA, van Zijl PC, Zhou J. Quantitative description of the asymmetry in magnetization transfer effects around the water resonance in the human brain. Magn Reson Med. 2007; 58:786–793. [PubMed: 17899597]
37. Scheidegger R, Vinogradov E, Alsop DC. Amide proton transfer imaging with improved robustness to magnetic field inhomogeneity and magnetization transfer asymmetry using

saturation with frequency alternating RF irradiation. Magn Reson Med. 2011; 66:1275–1285. [PubMed: 21608029]

38. Scheidegger, R.; Wong, E.; Alsop, D. Contributors to contrast between glioma and brain tissue in chemical exchange saturation transfer sensitive imaging at 3 Tesla; In the 3rd International Workshop on CEST Imaging; Annapolis, MD, USA. 2012.
39. Jin T, Wang P, Zong X, Kim SG. MR imaging of the amide-proton transfer effect and the pH-insensitive nuclear Overhauser effect at 9.4 T. Magn Reson Med. 2013; 69:760–770. [PubMed: 22577042]
40. Liu, D.; Zhou, J.; Xue, R.; Zuo, Z.; An, J.; Wang, DJ. RF power dependence of human brain CEST, NOE and metabolite MT effects at 7 T; In Proceedings of the 20th Annual Meeting of ISMRM; Melbourne, Australia. 2012. p. 745
41. Jones CK, Polders D, Hua J, Zhu H, Hoogduin HJ, Zhou J, Luijten P, van Zijl PC. In vivo three-dimensional whole-brain pulsed steady-state chemical exchange saturation transfer at 7 T. Magn Reson Med. 2012; 67:1579–1589. [PubMed: 22083645]
42. Hwang TL, van Zijl PC, Mori S. Accurate quantitation of water-amide proton exchange rates using the phase-modulated CLEAN chemical EXchange (CLEANEX-PM) approach with a Fast-HSQC (FHSQC) detection scheme. J Biomol NMR. 1998; 11:221–226. [PubMed: 9679296]
43. Bax A, Sklenar V, Summers MF. Direct identification of relayed nuclear Overhauser effects. J Magn Reson. 1986; 70:327–331.
44. Mori S, Eleff SM, Pilatus U, Mori N, van Zijl PC. Proton NMR spectroscopy of solvent-saturable resonances: a new approach to study pH effects in situ. Magn Reson Med. 1998; 40:36–42. [PubMed: 9660550]
45. Otting G, Liepinsh E, Wuthrich K. Protein hydration in aqueous solution. Science. 1991; 254:974–980. [PubMed: 1948083]
46. Kim M, Gillen J, Landman BA, Zhou J, van Zijl PC. Water saturation shift referencing (WASSR) for chemical exchange saturation transfer (CEST) experiments. Magn Reson Med. 2009; 61:1441–1450. [PubMed: 19358232]
47. Zu Z, Janve VA, Li K, Does MD, Gore JC, Gochberg DF. Multi-angle ratiometric approach to measure chemical exchange in amide proton transfer imaging. Magn Reson Med. 2012; 68:711–719. [PubMed: 22161770]
48. Vavasour IM, Whittall KP, Li DK, MacKay AL. Different magnetization transfer effects exhibited by the short and long T(2) components in human brain. Magn Reson Med. 2000; 44:860–866. [PubMed: 11108622]
49. Desmond KL, Stanisz GJ. Understanding quantitative pulsed CEST in the presence of MT. Magn Reson Med. 2012; 67:979–990. [PubMed: 21858864]
50. Zhou J, Payen JF, Wilson DA, Traystman RJ, van Zijl PC. Using the amide proton signals of intracellular proteins and peptides to detect pH effects in MRI. Nat Med. 2003; 9:1085–1090. [PubMed: 12872167]
51. Wilhelm MJ, Ong HH, Wehrli SL, Li C, Tsai PH, Hackney DB, Wehrli FW. Direct magnetic resonance detection of myelin and prospects for quantitative imaging of myelin density. Proc Natl Acad Sci USA. 2012; 109:9605–9610. [PubMed: 22628562]
52. Ceckler TL, Balaban RS. Tritium-proton magnetization transfer as a probe of cross relaxation in aqueous lipid bilayer suspensions. J Magn Reson. 1991; 93:572–588.
53. Henkelman RM, Stanisz GJ, Graham SJ. Magnetization transfer in MRI: a review. NMR Biomed. 2001; 14:57–64. [PubMed: 11320533]
54. Sled JG, Pike GB. Quantitative interpretation of magnetization transfer in spoiled gradient echo MRI sequences. J Magn Reson. 2000; 145:24–36. [PubMed: 10873494]
55. Liepinsh E, Otting G. Proton exchange rates from amino acid side chains—implications for image contrast. Magn Reson Med. 1996; 35:30–42. [PubMed: 8771020]
56. Segawa T, Kateb F, Duma L, Bodenhausen G, Pelupessy P. Exchange rate constants of invisible protons in proteins determined by NMR spectroscopy. Chembiochem. 2008; 9:537–542. [PubMed: 18247446]

57. Ng MC, Hua J, Hu Y, Luk KD, Lam EY. Magnetization transfer (MT) asymmetry around the water resonance in human cervical spinal cord. J Magn Reson Imaging. 2009; 29:523–528. [PubMed: 19243033]
58. Sun PZ, Benner T, Kumar A, Sorensen AG. Investigation of optimizing and translating pH-sensitive pulsed-chemical exchange saturation transfer (CEST) imaging to a 3 T clinical scanner. Magn Reson Med. 2008; 60:834–841. [PubMed: 18816867]
59. Graham SJ, Henkelman RM. Pulsed magnetization transfer imaging: evaluation of technique. Radiology. 1999; 212:903–910. [PubMed: 10478264]
60. Wolff SD, Balaban RS. Magnetization transfer contrast (MTC) and tissue water proton relaxation in vivo. Magn Reson Med. 1989; 10:135–144. [PubMed: 2547135]
61. Yarnykh VL. Pulsed Z-spectroscopic imaging of cross-relaxation parameters in tissues for human MRI: theory and clinical applications. Magn Reson Med. 2002; 47:929–939. [PubMed: 11979572]
62. Graham SJ, Henkelman RM. Understanding pulsed magnetization transfer. J Magn Reson Imaging. 1997; 7:903–912. [PubMed: 9307918]
63. Portnoy S, Stanisz GJ. Modeling pulsed magnetization transfer. Magn Reson Med. 2007; 58:144–155. [PubMed: 17659607]
64. Li JG, Graham SJ, Henkelman RM. A flexible magnetization transfer line shape derived from tissue experimental data. Magn Reson Med. 1997; 37:866–871. [PubMed: 9178237]
65. Woessner DE, Zhang S, Merritt ME, Sherry AD. Numerical solution of the Bloch equations provides insights into the optimum design of PARACEST agents for MRI. Magn Reson Med. 2005; 53:790–799. [PubMed: 15799055]
66. Ramani A, Dalton C, Miller DH, Tofts PS, Barker GJ. Precise estimate of fundamental in-vivo MT parameters in human brain in clinically feasible times. Magn Reson Imaging. 2002; 20:721–731. [PubMed: 12591568]
67. Li AX, Hudson RH, Barrett JW, Jones CK, Pasternak SH, Bartha R. Four-pool modeling of proton exchange processes in biological systems in the presence of MRI-paramagnetic chemical exchange saturation transfer (PARACEST) agents. Magn Reson Med. 2008; 60:1197–1206. [PubMed: 18958857]
68. Horch R, Gore J, Does M. Origins of the ultrashort-T2 1H NMR signals in myelinated nerve: a direct measure of myelin content? Magn Reson Med. 2011; 66:24–31. [PubMed: 21574183]
69. Helms G, Hagberg GE. Pulsed saturation of the standard two-pool model for magnetization transfer. I. The steady state. Concepts Magn Reson A. 2004; 21:37–49.
70. Goffeney N, Bulte JW, Duyn J, Bryant LH Jr, van Zijl PC. Sensitive NMR detection of cationic-polymer-based gene delivery systems using saturation transfer via proton exchange. J Am Chem Soc. 2001; 123:8628–8629. [PubMed: 11525684]
71. Friedman JI, McMahon MT, Stivers JT, Van Zijl PC. Indirect detection of labile solute proton spectra via the water signal using frequency-labeled exchange (FLEX) transfer. J Am Chem Soc. 2010; 132:1813–1815. [PubMed: 20095603]
72. de Graaf RA, Brown PB, McIntyre S, Nixon TW, Behar KL, Rothman DL. High magnetic field water and metabolite protonT1 andT2 relaxation in rat brain in vivo. Magn Reson Med. 2006; 56:386–394. [PubMed: 16767752]
73. Englander SW, Kallenbach NR. Hydrogen exchange and structural dynamics of proteins and nucleic acids. Q Rev Biophys. 1983; 16:521–655. [PubMed: 6204354]
74. Jones CK, Huang A, Xu J, et al. Nuclear Overhauser enhancement (NOE) imaging in the human brain at 7 T. NeuroImage C. 2013; 77:114–124.
75. Kim SG, Tsekos NV. Perfusion imaging by a flow-sensitive alternating inversion recovery (FAIR) technique application to functional brain imaging. Magn Reson Med. 1997; 37:425–435. [PubMed: 9055234]
76. Vinogradov E, Soesbe TC, Balschi JA, Dean Sherry A, Lenkinski RE. pCEST: positive contrast using chemical exchange saturation transfer. J Magn Reson. 2012; 215:64–73. [PubMed: 22237630]
77. Lee JS, Regatte RR, Jerschow A. Isolating chemical exchange saturation transfer contrast from magnetization transfer asymmetry under two-frequency rf irradiation. J Magn Reson. 2012; 215:56–63. [PubMed: 22237631]

78. Narvainen J, Hubbard PL, Kauppinen RA, Morris GA. Z-spectroscopy with alternating-phase irradiation. J Magn Reson. 2010; 207:242–250. [PubMed: 20920868]

79. Song X, Gilad AA, Joel S, et al. CEST phase mapping using a length and offset varied saturation (LOVARS) scheme. Magn Reson Med. 2012; 68:1074–1086. [PubMed: 22246684]

80. Zu Z, Janve VA, Xu J, Does MD, Gore JC, Gochberg DF. A new method for detecting exchanging amide protons using chemical exchange rotation transfer. Magn Reson Med. 2012; 69:637–647. [PubMed: 22505325]

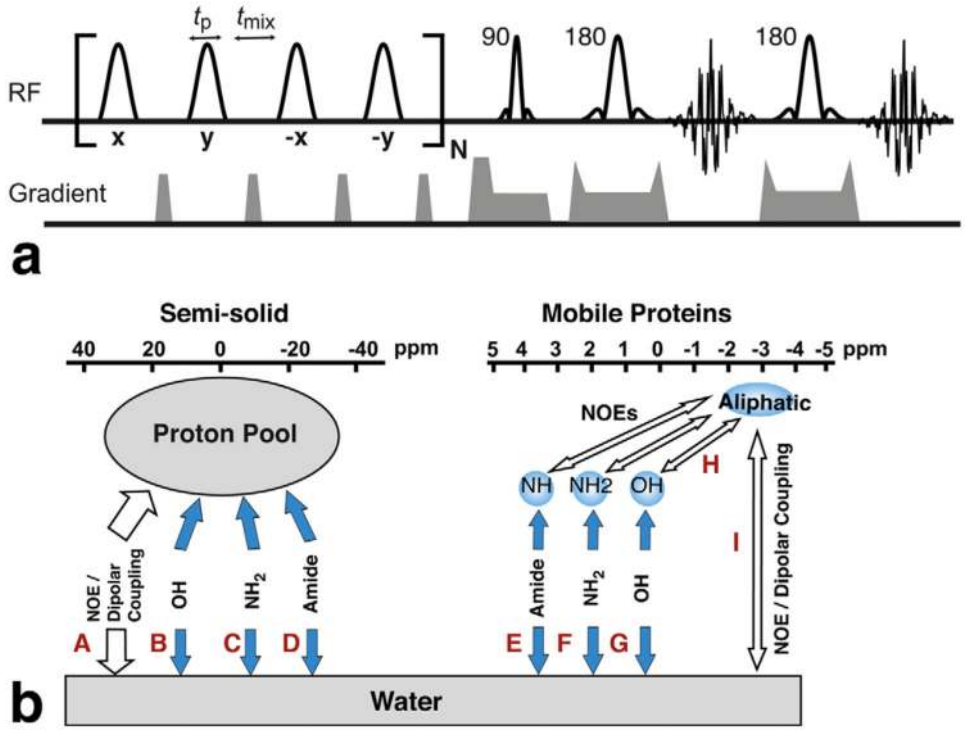

Fig. 1.

a: The VDMP-CEST sequence is composed of a train of Gaussian 180° pulses followed by an MRI readout (here a multispin echo sequence). The pulse width is t_p and the inter pulse delay t_{mix}. CYCLOPS phase cycling of the 180° pulses is applied together with crusher gradients during t_{mix} to suppress residual transverse magnetization. **b**: Possible pathways of magnetization transfer in semi-solid macromolecules and mobile proteins/peptides. The approximate chemical shift range of the proton groups is indicated too. The semi-solid component is treated as a single spin-bath with short a T_2 value. All chemical shift values used in this article are referenced to the water resonance frequency. A variety of spectroscopically distinct proton groups is present in mobile proteins, such as amide protons around 3.6 ppm and aliphatic/olefinic protons covering 0 ppm to −5 ppm. Chemical exchange between exchangeable protons and water is indicated using blue arrows, while the magnetization transfer due to NOE or dipole coupling is indicated using white arrows.

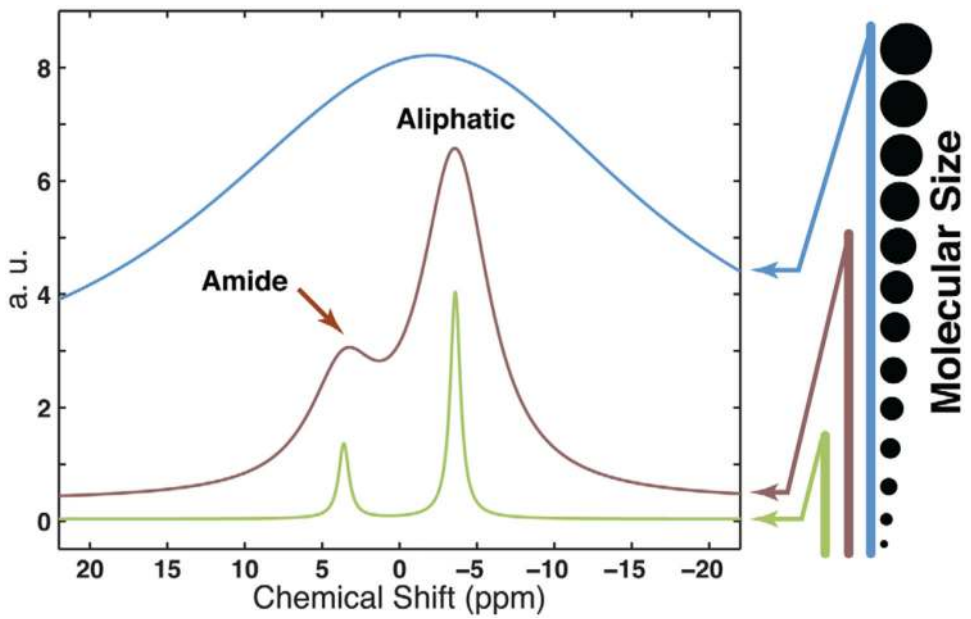

Fig. 2.

Illustration of MTC/CEST spectra from proteins/lipids with different mobility, i.e. different T_2 values. In the plot, the strong water signal is not shown for clarity. When weak RF pulses are applied in VDMP-CEST, the CEST spectrum arises mainly from mobile proteins/lipids with long T_2 values and the amide and aliphatic/olefinic peaks are two well separated groups (dotted green line). When higher saturation power is applied, more and more large molecules will be observed, and the amide and aliphatic peaks will overlap partially (dashed line). The CEST signal is not specific any more. At the strong saturation power extreme, almost all protons are observed including some with very short T_2 value, and the VDMP-CEST spectrum will be a single broad line including both the amide and aliphatic protons (solid line). The spectrum becomes the conventional MTC signal. In the simulation, the line broadening due to direct saturation was not included.

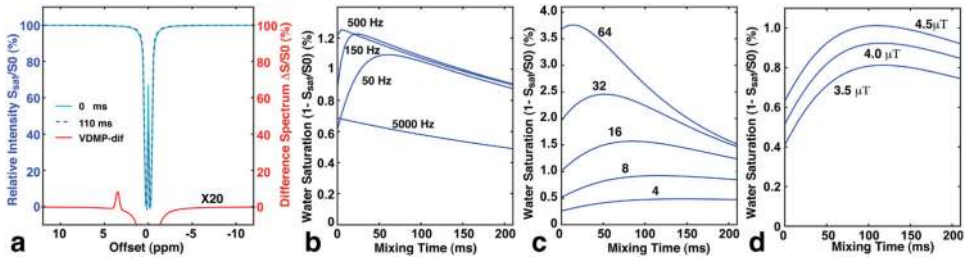

Fig. 3.

Simulated Z-spectra (**a**) and VDMP SI curves (**b**–**d**) for a VDMP-CEST sequence (6.9 ms pulses of B_1 =4 μ*T*) obtained using two-pool Bloch equations (70 mM amide protons, corresponding to a fraction of 6.36×10^{-4}, T_{1s} = 1 s, T_{2s} = 20 ms; water pool: T_{1w} = 2 s and T_{2w} = 35 ms). a: Z-spectra and VDMP difference spectrum (VDMP-dif) for exchange rate *k* of 20 Hz, mixing times 0 ms and 110 ms and eight Gaussian pulses with B_1 = 4 μT. The VDMP difference spectrum corresponds to a clean CEST (APT) spectrum. The difference spectrum was enlarged by a factor of 20 for clarity. b: VDMP SI curves for eight Gaussian pulses with B_1 = 4 μT and amide protons with exchange rates ranging from 50 Hz to 5000 Hz. **c**: VDMP SI curves for amide protons as a function of number of Gaussian pulses (B_1 = 4 μT) for *k* = 20 Hz. **d**: VDMP SI curves for amide protons as a function of B_1 using eight pulses and *k* = 20 Hz.

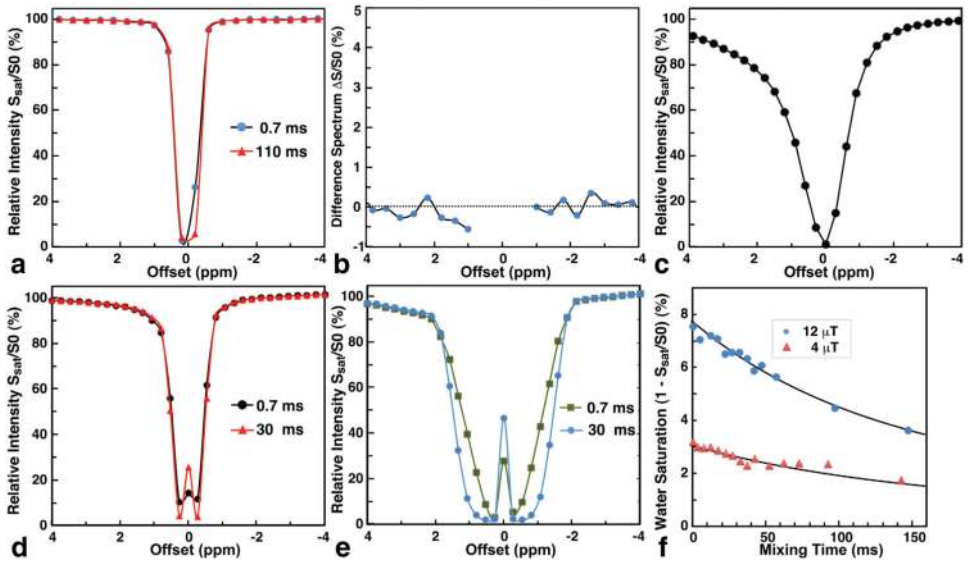

Fig. 4.

Saturation spectra for the glutamate phantom (12.5 mM, pH = 7.3) in PBS. **a**: Experimental VDMP-CEST Z-spectrum recorded using eight Gaussian inversion pulses with 4 μT peak power with mixing times 0.7 ms (blue circle) and 110 ms (red triangle), respectively. **b**: Corresponding VDMP difference spectrum. **c**: Conventional Z-spectrum recorded using a 2 s continuous wave saturation pulse with 2 μT power. **d**: VDMP-CEST Z-spectrum recorded using 32 Gaussian inversion pulses with 4 μT peak power with mixing times 0.7 ms (black circle) and 30 ms (red triangle), respectively. **e**: VDMP-CEST Z-spectrum recorded using 32 Gaussian inversion pulses with 12 μT peak power with mixing times 0.7 ms (green square) and 30 ms (blue circle), respectively. **f**: Experimental VDMP-CEST build-up curves at a frequency of 2.5 ppm from data recorded using 32 Gaussian inversion pulses. The solid line is the fit using the two-pool Bloch equations with $T_{1w}^{*}=2.5s$, T_{2w} = 110 ms, T_{1glu} = 2 s and T_{2glu} = 2 ms, and exchange rate 6 kHz. Note the lack of a buildup to equilibrium due to the reaching of maximum saturation at very short t_{mix} for these rapidly exchanging protons, followed by relaxation decay.

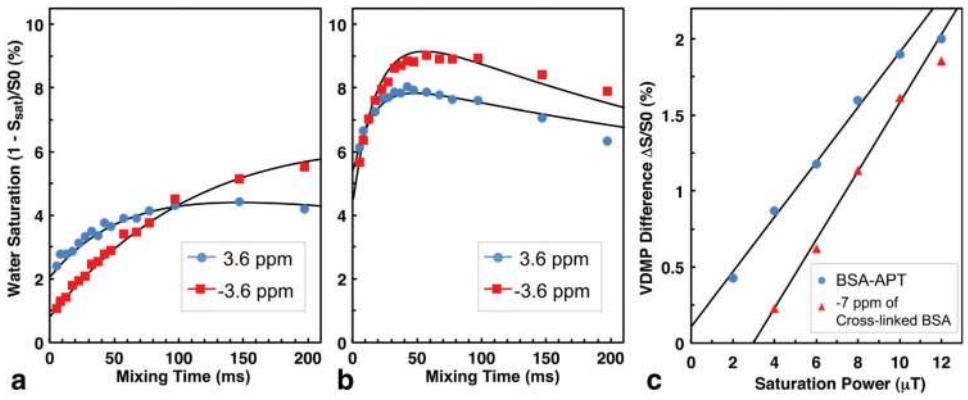

Fig. 5.

VDMP SI curves for 10% BSA in solution (**a**) and crosslinked (**b**) obtained using a VDMP-CEST sequence with eight Gaussian pulses and B_1 = 4 μT (200 Hz bandwidth). The solid lines are fits obtained using the two-pool Bloch equations assuming T_{2s} = 20 ms for BSA solution and T_{2s} = 0.13 ms for crosslinked BSA. Here T_{2s} for crosslinked BSA was determined by fitting the VDMP difference spectrum in Figure 6. The T_{1w}^{*} values were fitted to be 2 s (BSA solution) and 1.8 s (crosslinked BSA), respectively. The significantly lower T_{1w}^{*} relaxation times compared to PBS buffer are due to the back exchange of the fast exchange protons. **c**: Saturation power dependence for an 8-pulse VDMP-CEST difference SI (between t_{mix} = 110 ms and 0.7 ms) at offsets 3.6 ppm (APT) and −7 ppm (MTC background signal). The two solid lines are drawn for visual guidance only.

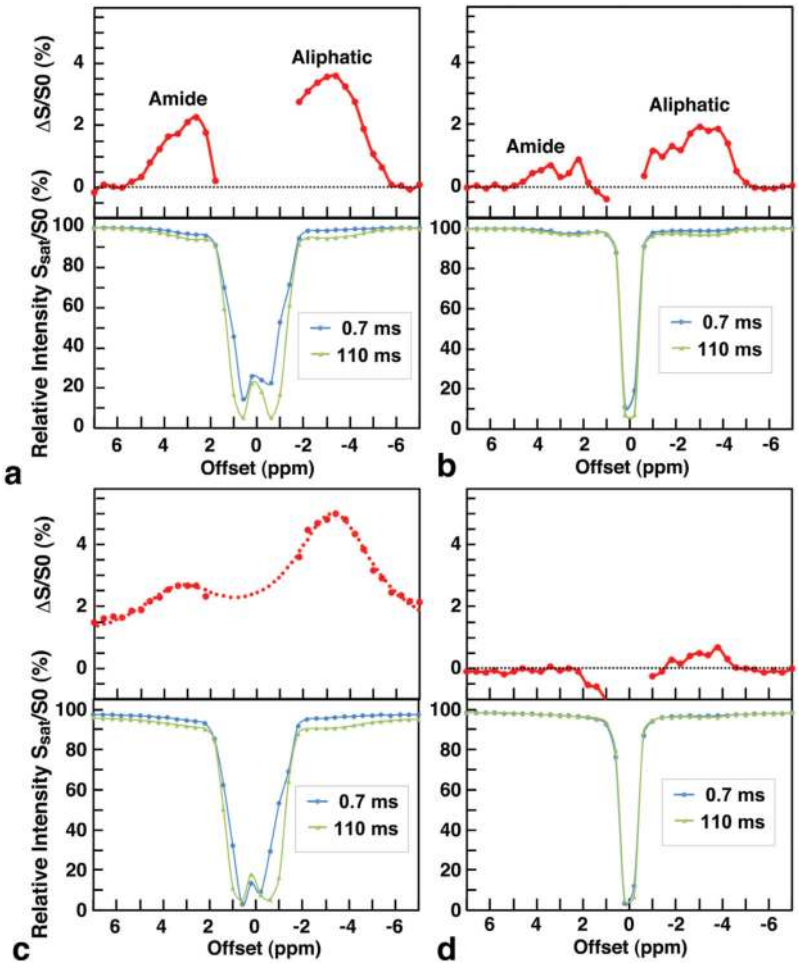

Fig. 6.

Mixing-time dependent Z-spectra (bottom) and corresponding VDMP-CEST difference spectra (top) for 10% BSA in solution (**a**,**b**) and crosslinked (**c**,**d**) obtained using a VDMP-CEST sequence with eight Gaussian inversion pulses. a,c: Spectra recorded with peak power 12 μT (2.3 ms length/600 Hz bandwidth); (b,d) spectra recorded with peak power 4 μT (6.9 ms length/200 Hz bandwidth). The CEST spectrum of the crosslinked BSA sample in (c) was fitted by assuming it arises from two pools of protons with offsets of ± 3.3 ppm (dashed line). T_{2s}= 0.13 ms. A ratio of 2.5 for aliphatic versus amide protons was obtained from the fitting.

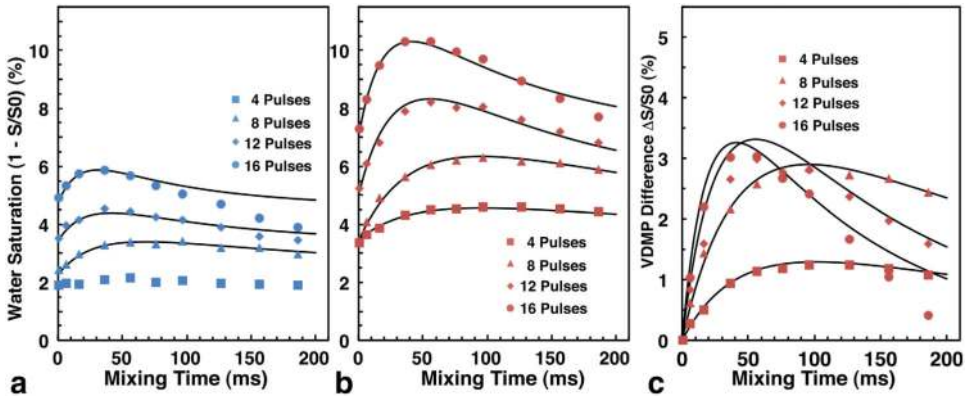

Fig. 7.

VDMP SI curves in rat brain cortex obtained using VDMP-CEST sequence at offsets of 3.6 ppm (**a**) and −3.6 ppm (**b**). **c**: The VDMP difference signal at the offset of −3.6 ppm together with the fitting curves are plotted with respect to mixing time. 2 μT saturation pulses (13.6 ms length, bandwidth 100 Hz, flip angle 180 degree) were applied. Exchange rates of 17 Hz (aliphatic) and 30 Hz (amide) were fitted (solid curves). In the fitting, $T_{1w}^{*}=2.5s$ (4 pulses), 1 s (8 pulses), 0.8 s (12 pulses) and 0.4 s (16 pulses) were used, while T_{2s} = 36 ms was used for both amide and aliphatic protons. The T_1 and T_2 of the exchangeable protons are all set to 1 s and 0.5 ms, respectively.

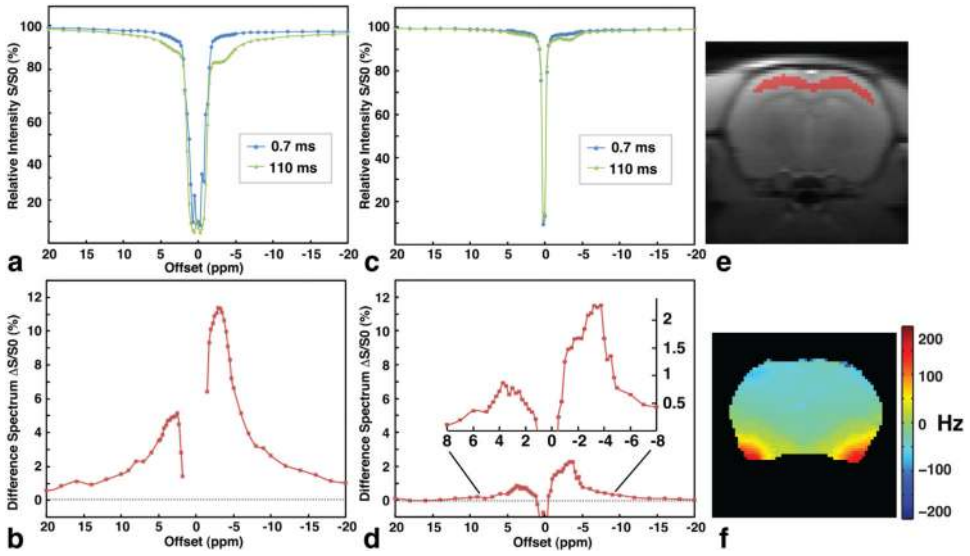

Fig. 8.

Mixing-time dependent Z-spectra for rat brain cortex recorded using eight Gaussian inversion pulses with B_1 levels of (**a**) 12 μT (2.3 ms length, eight pulses) and (**c**) 2 μT (13.8 ms length, eight pulses). The corresponding VDMP-CEST difference spectra are plotted in (**b**) and (**d**), respectively. E: The rat brain ROI from which the Z-spectra were obtained. **f**: A typical B_0 map recorded using the water saturation shift referencing sequence. The B_0 inhomogeneity is less than 150 Hz over the whole brain slice.

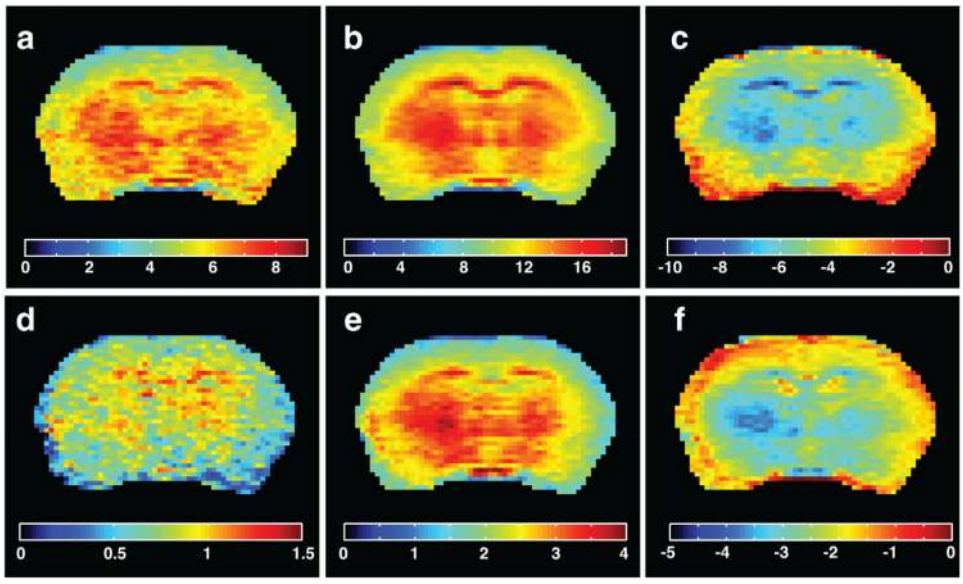

Fig. 9.

CEST images of rat brain recorded using B_1 = 12 μT (**a**–**c**) and 2 μT (**d**–**f**). These are VDMP-CEST difference images at offsets 3.6 ppm (a,d) and −3.6 ppm (**b,e**) as well as MTR_{asym} images (c,f). The VDMP difference images were obtained from [S(110 ms) − S(0.7 ms)]/$S0$, while the MTR_{asym} images reflect (S_{-36} − S_{36})/$S0$, in which S_{-36} and S_{36} are the image intensities recorded with eight pulses and 110 ms mixing time at offsets −3.6 ppm and 3.6 ppm, respectively. The VDMP image contrast at 12 μT is similar at the two frequencies (a,b), most likely due to the contribution of semi-solid species. At the lower peak power of 2 μT, the images at offsets 3.6 ppm (d) and −3.6 ppm (e) most likely reflect clean-APT and NOE-CEST effects. The MTR_{asym} images show the typical cortical gray matter to white matter contrast with the cortex more hyperintense. Eight averages were acquired to enhance the SNR for the images recorded with 2 μT Notice the different color scales.